Optimum tuning of series and parallel LR circuits for passive vibration suppression using piezoelectric elements

Keisuke Yamada*, Hiroshi Matsuhisa, Hideo Utsuno, Katsutoshi Sawada

Department of Mechanical Engineering and Science, Kyoto University, Yoshida-Honmachi, Sakyo-ku, Kyoto 606-8501, Japan

ARTICLE INFO

ABSTRACT

Bending vibration of flexible structures can be suppressed passively using piezoelectric electromechanical transducers and optimally tuned LR circuits. Since these systems include both mechanical and electrical elements, the governing equations consist of electrically coupled equations of motion. This paper describes a new method for deriving the governing equations that describe a system's vibration suppression based on the equilibrium of force principle and using an equivalent mechanical model of a piezoelectric element. Both series and parallel LR circuits are considered in the modeling approach. The optimum values for a mechanical vibration absorber can be formulated by using the two fixed points method. However, exact optimal values for the resistances of the LR circuits have not been formulated in the research literature thus far, and approximate values have been used. Analytical formulations are derived in this paper, and optimum values of the LR circuits are presented, not only in displacement, but also in terms of velocity and acceleration. The effects of the stiffness of the adhesive bond between the host structure and piezoelectric element, the dielectric loss in a piezoelectric element, and the internal resistance of an inductor are considered in the theoretical analysis. The effectiveness of the described analytical method is validated through simulations and experiments.

© 2010 Elsevier Ltd. All rights reserved.

1. Introduction

Suppression of bending vibration using piezoelectric elements has attracted the attention of many researchers. Typically, thin ceramic plates of piezoelectric material are used because this configuration requires minimal additional space and they are easy to install. In contrast, vibration suppression devices such as mechanical vibration absorbers usually need a significant amount of space and require a system level integration approach. Both active vibration control [1,2] and passive vibration suppression [3–7] using piezoelectric elements have been investigated in the research literature. Several hybrid methods [8–11] have also been proposed. Active vibration control is often more effective than passive vibration suppression for a given device size, but they suffer from stability problems. In principle, passive methods are stable and offer a higher degree of simplicity in their implementation. For these reasons, passive vibration suppression using tuned LR circuits is the focus of this paper.

In previous works, it has been shown that both series and parallel LR circuits are effective in passively absorbing vibration using piezoelectric elements [4,6]. Fundamental characterization of piezoelectric vibration absorbers and passive

---

* Corresponding author. Tel./fax: +81 75 753 5195.
  E-mail address: keisu@t01.mbox.media.kyoto-u.ac.jp (K. Yamada).

LR circuits has been shown; however, significant work remains in specific areas. In particular, the characteristics of the piezoelectric elements have not been thoroughly included in the derivation of governing equations, and as a result, the mechanism for how the controlling force is generated by LR circuits has not been illustrated in detail. In addition, accurate formulations for obtaining optimum values for the resistances, which agree with the two fixed points method [12], have not been derived thus far. The differences in performance between series and parallel LR circuits should be investigated more closely. In the research literature, the optimum LR values for the circuits were derived only with respect to displacement even though the vibration of the host structure is often evaluated in terms of velocity or acceleration. Finally, the results of pure theoretical analysis and experiment often do not agree well in the research literature, especially in terms of the equivalent stiffness ratio of the piezoelectric element and the optimum value of resistance. To address these issues, this paper derives the governing equations by using a new equivalent mechanical model of a piezoelectric element. An equivalent model of a piezoelectric element proposed previously consists of frequency-dependent elements [13]; however, the proposed equivalent model consists of frequency-independent elements. Using the two fixed points method, accurate formulations for the optimum values of the LR circuits are derived, not only in terms of displacement but also in terms of velocity and acceleration. Using these formulations, the performance and optimum values of series and parallel LR circuits are compared theoretically. Finally, the dielectric loss of a piezoelectric element, internal resistance of the inductor, and stiffness of the adhesive bond are modeled theoretically. The effectiveness of the theoretical analysis is verified in simulations and experiments.

2. Theoretical analysis

2.1. Piezoelectric constitutive equations and equivalent mechanical model

Piezoelectric elements generate electrical voltage when they are strained. This phenomenon is called the piezoelectric effect. The inverse piezoelectric effect occurs when a piezoelectric element strains in response to an applied voltage. A piezoelectric element can be used as both a sensor and an actuator by using these responses. Piezoelectric elements can be categorized into several types according to the directions of polarization and strain. There is no essential difference between them and general formulations will be developed throughout this work. A plate type of piezoelectric elements used in this paper is usually used for bending vibration suppression. As shown in Fig. 1, directions of polarization and strain of the plate type are perpendicular to each other. The piezoelectric constitutive equations are given as

$$S_1 = s_{11}^E T_1 + d_{31} E_3, \tag{1}$$

$$D_3 = d_{31} T_1 + \varepsilon_{33}^T E_3, \tag{2}$$

where S_1 is the strain, T_1 is the stress, E_3 is the electrical field, D_3 is the electrical displacement, s_{11}^E is the elastic compliance defined as the reciprocal of Young's modulus, d_{31} is the piezoelectric constant, and ε_{33}^T is the electrical permittivity. The subscripts 1 and 11 denote the longitudinal direction, 3 and 33 denote the thickness direction, and 31 denote that the electrical displacement is the thickness direction and the strain is the longitudinal direction. The superscripts E and T denote the values which are obtained under constant electrical field and constant stress, respectively. The strain in width direction and the mass of the piezoelectric element are ignored here for simplicity. Eqs. (1) and (2) describe the inverse piezoelectric effect and piezoelectric effect, respectively. Eqs. (1) and (2) can be transformed into the following equations:

$$x_1 = \frac{1}{E_p} \frac{l_p}{w_p t_p} F_1 + d_{31} \frac{l_p}{t_p} V_3, \tag{3}$$

$$q_3 = d_{31} \frac{l_p}{t_p} F_1 + \varepsilon_{33}^T \frac{l_p w_p}{t_p} V_3, \tag{4}$$

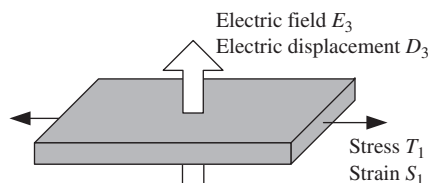$$x_1 = l_p S_1, \quad q_3 = l_p w_p D_3, \quad F_1 = w_p t_p T_1, \quad V_3 = t_p E_3, \tag{5-8}$$

Fig. 1. Schematic diagram of a plate type piezoelectric element.

where F_1 is the force, V_3 is the voltage, x_1 is the displacement, q_3 is the charge, E_p is Young's modulus defined as reciprocal of s_{11}^E, l_p, w_p, and t_p are the length, width, and thickness, respectively. Eqs. (3) and (4) are simplified as

$$x_1 = \frac{1}{k_p}F_1 + \frac{\theta_p}{k_p}V_3, \tag{9}$$

$$q_3 = \frac{\theta_p}{k_p}F_1 + C_p^T V_3, \tag{10}$$

$$k_p = E_p \frac{w_p t_p}{l_p}, \quad \theta_p = d_{31}E_p w_p, \quad C_p^T = \varepsilon_{33}^T \frac{l_p w_p}{t_p}, \tag{11–13}$$

where k_p is the longitudinal mechanical stiffness, θ_p is the elemental electromechanical coupling coefficient, and C_p^T is the capacitance under constant stress. From Eqs. (9) and (10), capacitance under constant strain is defined as follows:

$$C_p^S = C_p^T - \frac{\theta_p^2}{k_p}, \tag{14}$$

where the superscript S denotes that the value is obtained under constant strain. Substituting Eq. (14) into Eq. (10) gives

$$q_3 = \frac{\theta_p}{k_p}F_1 + \left(\frac{\theta_p^2}{k_p} + C_p^S\right)V_3 = \theta_p x_1 + C_p^S V_3. \tag{15}$$

From Eqs. (9) and (15), the equivalent mechanical model is drawn as Fig. 2(a). Here $1/\overline{C}_p^S$ is the spring constant, $\overline{\theta}_p$ is the area ratio between the upper and right pistons, $\overline{V}_3$ is the force, $\overline{q}_3$ is the displacement. The values of $\overline{C}_p^S$, $\overline{\theta}_p$, $\overline{V}_3$, and $\overline{q}_3$ are equal to the values of C_p^S, θ_p, V_3, and q_3, respectively. The left half of the equivalent model (a) is the mechanical stiffness given by Eq. (11), and the right half shows the electrical properties of the transducer used to convert between mechanical and electrical energy. The volume in the cylinder is constant, and the pressure in the cylinder is uniform. The cylinder is fixed, and does not move. The equivalent mechanical model (a) can be transformed into the mechanical model (b). In this paper, the equivalent mechanical models (a) and (b) shown in Fig. 2 are referred to subsequently as imaginary equivalent mechanical model and the perfect equivalent mechanical model, respectively. The stiffness of the electrical part is written as

$$k_z = \frac{\theta_p^2}{C_p^S} = \frac{\overline{\theta}_p^2}{\overline{C}_p^S} = \frac{d_{31}^2 E_p}{\varepsilon_{33}^T - d_{31}^2 E_p}k_p. \tag{16}$$

Eq. (16) implies that the stiffness of the electrical part is proportional to the stiffness of the mechanical part. The original and equivalent mechanical models, when electrical impedance Z_e is coupled to the piezoelectric element, are shown in Fig. 3. The electrical impedance Z_e is shown as the mechanical impedance $\overline{Z}_e$ in the imaginary equivalent mechanical model and transformed into the mechanical impedance Z_m in the perfect equivalent mechanical model. The mechanical impedance Z_m is written as follows:

$$Z_m = Z_e \theta_p^2 = \overline{Z}_e \overline{\theta}_p^2. \tag{17}$$

The lower end of the equivalent stiffness k_z in Fig. 3(b) is free when the electrodes of the piezoelectric element are shorted, and fixed when the electrodes are opened. When the electrodes are shorted, the electrical property of the piezoelectric element does not have any physical effect.

2.2. Governing equations

An example model of for application of vibration suppression using a piezoelectric element and electrical impedance Z_e is shown in Fig. 4. In this case, the cantilever is the host structure that is experiencing vibration suppression, and it is
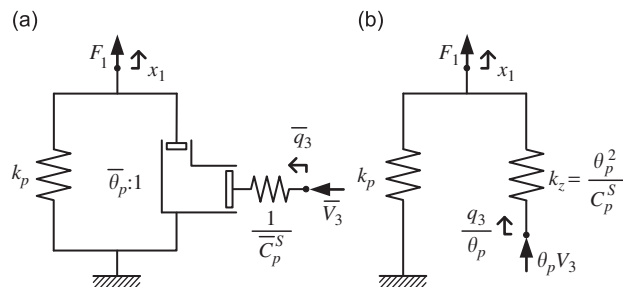

Fig. 2. Equivalent mechanical models of a piezoelectric element: (a) imaginary model and (b) perfect model.
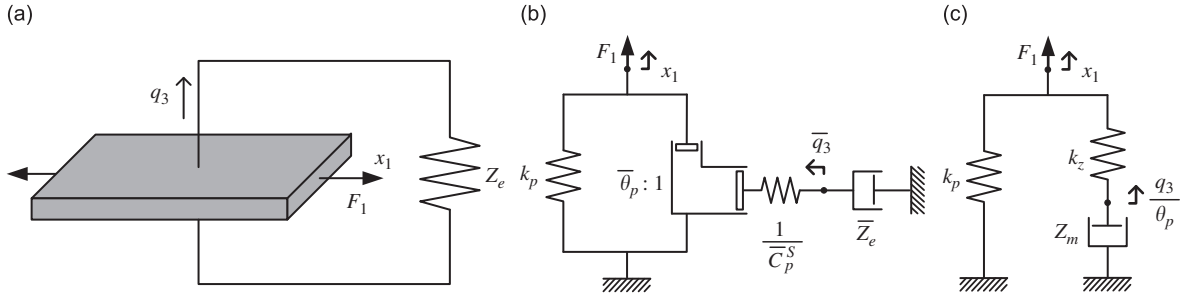
Fig. 3. Original and equivalent mechanical models of a piezoelectric element with electrical impedance: (a) original model, (b) imaginary model, and (c) perfect model.
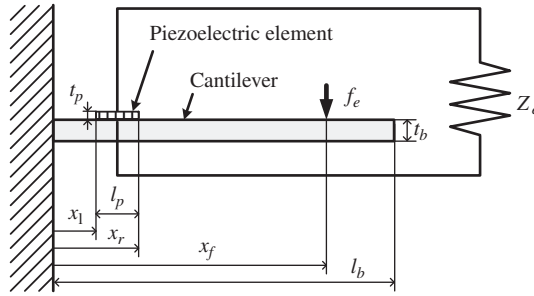

Fig. 4. A model of vibration suppression using a piezoelectric element and electrical impedance.

excited by external force f_e. The piezoelectric element is attached to the host structure with an adhesive bond. Vibration suppression using a tuned LR circuit can suppress only a single vibration mode. Therefore, the frequency range considered in this analysis is around the natural frequency of the targeted vibration mode, and the other vibration modes are ignored in theoretical analysis. In this case, their influences are small. The equation of motion when the electrodes of the piezoelectric element are shorted is written as follows:

$$M\ddot{\xi}+K\xi=B_f f_e,\tag{18}$$

$$M=M_b+M_p=1,\tag{19}$$

$$M_b=\rho_b w_b t_b\int_0^{l_b}\psi^2\,dx,\tag{20}$$

$$M_p=\rho_p w_p t_p\int_{x_l}^{x_r}\psi^2\,dx,\tag{21}$$

$$K=K_b+K_p,\tag{22}$$

$$K_b=E_b w_b\left[\int_0^{x_l}\int_{-(1/2)t_b}^{(1/2)t_b}z^2\left(\frac{\partial^2\psi}{\partial x^2}\right)^2dz\,dx+\int_{x_l}^{x_r}\int_{-(t_b-t_n)}^{t_n}z^2\left(\frac{\partial^2\psi}{\partial x^2}\right)^2dz\,dx+\int_{x_r}^{l_b}\int_{-(1/2)t_b}^{(1/2)t_b}z^2\left(\frac{\partial^2\psi}{\partial x^2}\right)^2dz\,dx\right],\tag{23}$$

$$K_p=E_p w_p\int_{x_l}^{x_r}\int_{t_n}^{t_n+t_p}z^2\left(\frac{\partial^2\psi}{\partial x^2}\right)^2dz\,dx,\tag{24}$$

$$B_f=\psi(x_f),\tag{25}$$

$$t_n=\frac{E_b w_b t_b^2-E_p w_p t_p^2}{2(E_b w_b t_b+E_p w_p t_p)},\tag{26}$$

where ξ is the modal displacement, ρ_b and ρ_p are the densities of the beam and the piezoelectric element, respectively, E_b is Young's modulus of the beam, l_b, w_b, t_b are the length, width, and thickness of the beam, respectively, t_n is the distance between the neutral axis and the adverse side of the beam within the range where the piezoelectric element is attached, x_l, x_r, x_f are the distance between the clamped end and the left and right endpoints of the piezoelectric element and the point
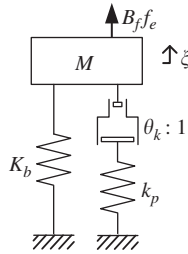
Fig. 5. Equivalent mechanical model of the targeted vibration mode with a short-circuited piezoelectric element.
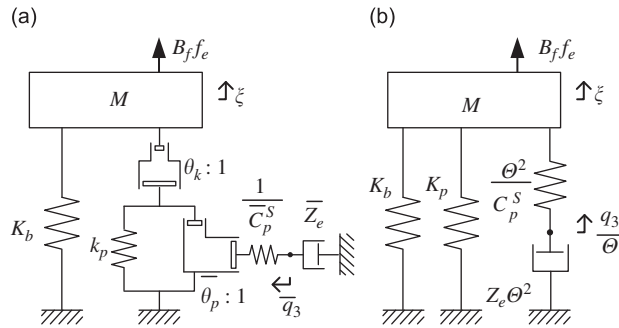

Fig. 6. Equivalent mechanical models of the targeted vibration mode with a piezoelectric element shunted by electrical impedance Z_e: (a) imaginary model and (b) perfect model.

where the external force is added, respectively, ψ is the shape function of the targeted vibration mode. The x-axis is the longitudinal direction and the origin is at the clamped end. The variable z denotes the distance from the neutral axis. Since this cantilever is thin, the shear deformation and rotary inertia of the cantilever are ignored. As written in Eq. (19), the shape function ψ used in this paper is normalized as the modal mass M becomes 1. When the electrodes are shorted, the electrical property of the piezoelectric element does not affect the system. The equation of motion (18) is derived from the simple mechanical model shown in Fig. 5. Here the cylinder is fixed in space, and the area ratio θ_k is written as

$$\theta_k = \sqrt{\frac{K_p}{k_p}}. \tag{27}$$

Because k_p and k_z are in the proportional relation from Eq. (16), the imaginary and perfect equivalent mechanical models when the electrodes of the piezoelectric element are shunted by the electrical impedance Z_e are drawn as Fig. 6. From these equivalent mechanical models, the governing equations are written as follows:

$$M\ddot{\xi} + K\xi + \Theta\left(\frac{\Theta}{C_p^S}\xi - \frac{1}{C_p^S}q_3\right) = B_f f_e, \tag{28}$$

$$Z_e\dot{q}_3 + \frac{1}{C_p^S}q_3 = \frac{\Theta}{C_p^S}\xi, \tag{29}$$

where Θ is the modal electromechanical coupling coefficient, and given as follows:

$$\Theta = \theta_p\theta_k. \tag{30}$$

2.3. Passive vibration suppression using an LR circuit

Models for passive vibration suppression using series and parallel LR circuits are shown in Fig. 7. Electrical impedances of the series and parallel LR circuits are written as

$$Z_e = \begin{cases} j\omega L + R & \text{(series)}, \\ \dfrac{j\omega LR}{j\omega L + R} & \text{(parallel)}, \end{cases} \tag{31}$$
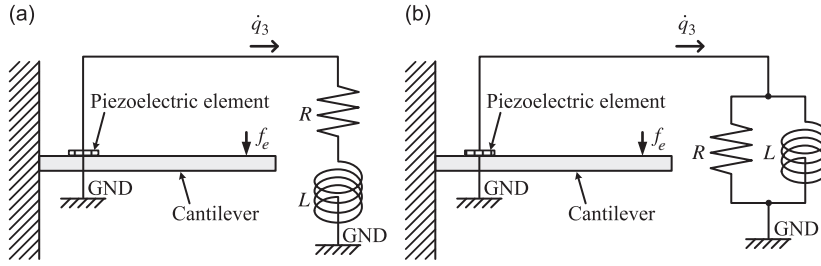
Fig. 7. Schematic diagrams of passive vibration suppression using series and parallel LR circuits: (a) series LR circuit and (b) parallel LR circuit.
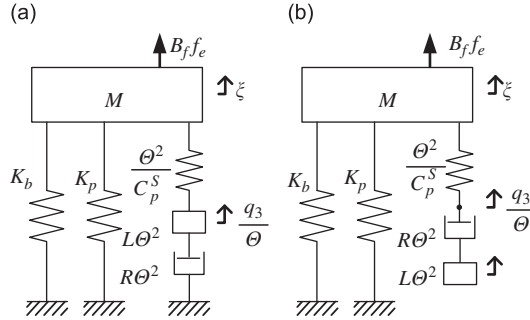

Fig. 8. Perfect equivalent mechanical models of passive vibration suppression using series and parallel LR circuits: (a) series LR circuit and (b) parallel LR circuit.

where j is the imaginary unit, ω is the excitation frequency, L is the inductance, and R is the resistance. The perfect equivalent mechanical models are depicted in Fig. 8. Compared to a typical mechanical vibration absorber, the positions of the dashpots are different. From Eqs. (28), (29) and (31), the nondimensional compliance is derived as

$$\frac{\Xi}{\Xi_{st}} = \begin{cases} \dfrac{1}{-g^2+1+\beta G_S} & \text{(series)}, \\ \dfrac{1}{-g^2+1+\beta G_P} & \text{(parallel)}, \end{cases} \tag{32}$$

$$G_S = \frac{-g^2+2j\zeta_S fg}{f^2-g^2+2j\zeta_S fg}, \tag{33}$$

$$G_P = \frac{-g^2}{f^2-g^2+2j\zeta_P fg}, \tag{34}$$

$$\Xi_{st} = \frac{B_f F_e}{K}, \quad g=\frac{\omega}{\Omega}, \quad \beta=\frac{\Theta^2}{KC_p^S}, \tag{35--37}$$

$$f=\frac{\omega_a}{\Omega}, \quad \zeta_S=\frac{R}{2}\sqrt{\frac{C_p^S}{L}}, \quad \zeta_P=\frac{1}{2R}\sqrt{\frac{L}{C_p^S}}, \quad \Omega=\sqrt{\frac{K}{M}}, \quad \omega_a=\sqrt{\frac{1}{LC_p^S}}. \tag{38--42}$$

Here Ξ and F_e are the complex amplitude of ξ and f_e, respectively. From Eq. (32), the magnitudes of the nondimensional compliance u_C, mobility u_M, and accelerance u_A are given as follows:

$$u_C = \left|\frac{\Xi}{\Xi_{st}}\right| = \begin{cases} \sqrt{\dfrac{a^2+4\zeta_S^2 b^2}{c^2+4\zeta_S^2 d_S^2}} & \text{(series)}, \\ \sqrt{\dfrac{a^2+4\zeta_P^2 b^2}{c^2+4\zeta_P^2 d_P^2}} & \text{(parallel)}, \end{cases} \tag{43}$$

$$u_M = \frac{1}{\Omega}\left|\frac{\dot{\Xi}}{\Xi_{st}}\right| = \begin{cases} \sqrt{\dfrac{g^2(a^2+4\zeta_S^2 b^2)}{c^2+4\zeta_S^2 d_S^2}} & \text{(series)}, \\[2em] \sqrt{\dfrac{g^2(a^2+4\zeta_P^2 b^2)}{c^2+4\zeta_P^2 d_P^2}} & \text{(parallel)}, \end{cases} \tag{44}$$

$$u_A = \frac{1}{\Omega^2}\left|\frac{\ddot{\Xi}}{\Xi_{st}}\right| = \begin{cases} \sqrt{\dfrac{g^4(a^2+4\zeta_S^2 b^2)}{c^2+4\zeta_S^2 d_S^2}} & \text{(series)}, \\[2em] \sqrt{\dfrac{g^4(a^2+4\zeta_P^2 b^2)}{c^2+4\zeta_P^2 d_P^2}} & \text{(parallel)}, \end{cases} \tag{45}$$

$$a = f^2 - g^2, \tag{46}$$

$$b = fg, \tag{47}$$

$$c = (1-g^2)(f^2-g^2) - \beta g^2, \tag{48}$$

$$d_S = fg(1-g^2+\beta), \tag{49}$$

$$d_P = fg(1-g^2), \tag{50}$$

$$\dot{\Xi} = j\omega\Xi, \tag{51}$$

$$\ddot{\Xi} = -\omega^2 \Xi. \tag{52}$$

2.3.1. Optimum tuning in compliance

The two fixed points method [12] is common for finding the optimum natural frequency ratio and the resistance ratio of the additional one degree of freedom system that minimizes the maximum amplitude in the frequency domain. The two fixed points method is often used in optimum tuning of mechanical vibration absorbers because of its simplicity; it is also applied to the optimum tuning of the series and parallel LR circuits in this paper.

Because the magnitude of the nondimensional compliance (43) has two fixed points that are independent of the resistance ratio, the optimum natural frequency ratio is determined so that amplitudes at the two fixed points become equal, and the optimum resistance ratio is derived so that amplitude is maximized at the two fixed points.

The optimum natural frequency ratio in the magnitude of the nondimensional compliance (43) is given for the condition that the amplitudes at two fixed points—given by A and B—are equal

$$f_{C_{opt}} = \begin{cases} \sqrt{1+\beta} & \text{(series)}, \\[1em] \sqrt{\dfrac{2-\beta}{2}} & \text{(parallel)}. \end{cases} \tag{53}$$

The nondimensional frequencies of the two fixed points are given as

$$g_{A,B} = \begin{cases} \sqrt{(1+\beta)\mp\sqrt{\dfrac{\beta(1+\beta)}{2}}} & \text{(series)}, \\[1.5em] \sqrt{1\mp\sqrt{\dfrac{\beta}{2}}} & \text{(parallel)}. \end{cases} \tag{54}$$

The amplitudes at the two fixed points are derived as follows:

$$u_C\big|_{g=g_{A,B}} = \begin{cases} \sqrt{\dfrac{2}{\beta(1+\beta)}} & \text{(series)}, \\[1.5em] \sqrt{\dfrac{2}{\beta}} & \text{(parallel)}. \end{cases} \tag{55}$$

The optimum resistance ratios at the two fixed points are given as

$$\begin{cases} \zeta_{SA,B} = \dfrac{1}{2}\sqrt{\left.\dfrac{-aa'+u_C^2 cc'}{bb'-u_C^2 d_S d_S'}\right|_{g=g_{A,B}}} & \text{(series)}, \\[4mm] \zeta_{PA,B} = \dfrac{1}{2}\sqrt{\left.\dfrac{-aa'+u_C^2 cc'}{bb'-u_C^2 d_P d_P'}\right|_{g=g_{A,B}}} & \text{(parallel)}, \end{cases} \tag{56}$$

where the prime $'$ denotes $\partial/\partial g$. ζ_A and ζ_B are not equal; however, the difference is minute. The arithmetic average, geometric average, and root mean square of ζ_A and ζ_B can all be used as the optimum resistance ratio because the difference between them is small enough to be ignored. In this paper, the optimum resistance ratio is defined by root mean square because of simplicity of the expression

$$\begin{cases} \zeta_{CS_{opt}} = \sqrt{\dfrac{\zeta_{SA}^2 + \zeta_{SB}^2}{2}} = \dfrac{1}{2}\sqrt{\dfrac{3\beta}{2+\beta}} & \text{(series)}, \\[4mm] \zeta_{CP_{opt}} = \sqrt{\dfrac{\zeta_{PA}^2 + \zeta_{PB}^2}{2}} = \dfrac{1}{2}\sqrt{\dfrac{3\beta}{2-\beta}} & \text{(parallel)}. \end{cases} \tag{57}$$

As indicated by Eqs. (53) and (57), both optimum natural frequency ratio and optimum resistance ratio are determined only by the equivalent stiffness ratio β.

2.3.2. Optimum tuning in mobility

Optimum values of the series and parallel LR circuits in terms of the magnitude of the nondimensional mobility can be derived by the two fixed points method as well as in terms of the magnitude of the nondimensional compliance. The optimum natural frequency ratio, the nondimensional frequencies of the two fixed points, the amplitudes at the two fixed points, and the optimum resistance ratio are given as follows:

$$f_{M_{opt}} = \begin{cases} (1+\beta)\sqrt{\dfrac{2}{2+\beta}} & \text{(series)}, \\[4mm] 1 & \text{(parallel)}, \end{cases} \tag{58}$$

$$g_{A,B} = \begin{cases} \sqrt{\dfrac{(1+\beta)\left[(4+3\beta)\mp\sqrt{\beta(8+5\beta)}\right]}{2(2+\beta)}} & \text{(series)}, \\[4mm] \sqrt{\dfrac{(4+\beta)\mp\sqrt{\beta(8+\beta)}}{4}} & \text{(parallel)}, \end{cases} \tag{59}$$

$$u_M\big|_{g=g_{A,B}} = \begin{cases} \sqrt{\dfrac{2+\beta}{\beta(1+\beta)}} & \text{(series)}, \\[4mm] \sqrt{\dfrac{2}{\beta}} & \text{(parallel)}, \end{cases} \tag{60}$$

$$\begin{cases} \zeta_{MS_{opt}} = \dfrac{1}{4}\sqrt{\dfrac{\beta(24+24\beta+5\beta^2)}{(1+\beta)(2+\beta)^2}} & \text{(series)}, \\[4mm] \zeta_{MP_{opt}} = \dfrac{1}{2}\sqrt{\dfrac{3\beta}{2}} & \text{(parallel)}. \end{cases} \tag{61}$$

2.3.3. Optimum tuning in acceleration

Optimum values of the series and parallel LR circuits for the magnitude of the nondimensional acceleration can be derived by the two fixed points method as well as for the magnitude of the nondimensional compliance. The optimum natural frequency ratio, the nondimensional frequencies of the two fixed points, the amplitudes at the two fixed points, and the optimum resistance ratio are given as follows:

$$f_{A_{opt}} = \begin{cases} 1+\beta & \text{(series)}, \\[2mm] \sqrt{\dfrac{2+\beta}{2}} & \text{(parallel)}, \end{cases} \tag{62}$$

$$g_{A,B} = \begin{cases} \sqrt{\dfrac{(1+\beta)\left[(2+\beta) \mp \sqrt{\beta(2+\beta)}\right]}{2}} & \text{(series)}, \\[3mm] \sqrt{\dfrac{(2+\beta) \mp \sqrt{\beta(2+\beta)}}{2}} & \text{(parallel)}, \end{cases} \tag{63}$$

$$u_{A}\big|_{g=g_{A,B}} = \begin{cases} \sqrt{\dfrac{2+\beta}{\beta}} & \text{(series)}, \\[3mm] \sqrt{\dfrac{2+\beta}{\beta}} & \text{(parallel)}, \end{cases} \tag{64}$$

$$\begin{cases} \zeta_{AS_{\mathrm{opt}}} = \dfrac{1}{2}\sqrt{\dfrac{3\beta}{2(1+\beta)}} & \text{(series)} \\[3mm] \zeta_{AP_{\mathrm{opt}}} = \dfrac{1}{2}\sqrt{\dfrac{3\beta}{2}} & \text{(parallel)} \end{cases}. \tag{65}$$

2.3.4. Optimum values of the inductance and the resistance

Using the optimum natural frequency ratio f_{opt} and the optimum resistance ratios $\zeta_{S_{\mathrm{opt}}}$ and $\zeta_{P_{\mathrm{opt}}}$, the optimum values of the inductance and the resistance are formulated as follows:

$$L_{\mathrm{opt}} = \frac{1}{f_{\mathrm{opt}}^{2}} \frac{1}{C_{p}^{S}} \frac{1}{\Omega^{2}}, \tag{66}$$

$$R_{\mathrm{opt}} = \begin{cases} 2\zeta_{S_{\mathrm{opt}}} \dfrac{1}{f_{\mathrm{opt}}} \dfrac{1}{C_{p}^{S}} \dfrac{1}{\Omega} & \text{(series)}, \\[3mm] \dfrac{1}{2\zeta_{P_{\mathrm{opt}}}} \dfrac{1}{f_{\mathrm{opt}}} \dfrac{1}{C_{p}^{S}} \dfrac{1}{\Omega} & \text{(parallel)}. \end{cases} \tag{67}$$

2.4. Comparison between series and parallel LR circuits

2.4.1. Performance comparison

The vibration suppression performance is evaluated based on the amplitude at the two fixed points because the amplitude at these points is maximized. The amplitudes at the two fixed points for the compliance, mobility, and accelerance are given by Eqs. (55), (60), and (64), respectively. The amplitudes are evaluated by using only the equivalent stiffness ratio β as an independent variable. The relationship between the amplitude at the two fixed points and the equivalent stiffness ratio β is shown in Fig. 9. The amplitude of a series LR circuit is smaller than that of a parallel LR circuit for the compliance and mobility, and they are equal in the accelerance. The amplitudes of series and parallel LR circuits are almost equal when the value of the equivalent stiffness ratio β is much smaller than 1.

The performance of a typical mechanical vibration absorber is evaluated based on the mass ratio. By contrast, the performance of vibration suppression using piezoelectric elements uses the stiffness ratio because the electrical properties of a piezoelectric element correspond to a spring in the equivalent mechanical model. However, the mass ratio can also be
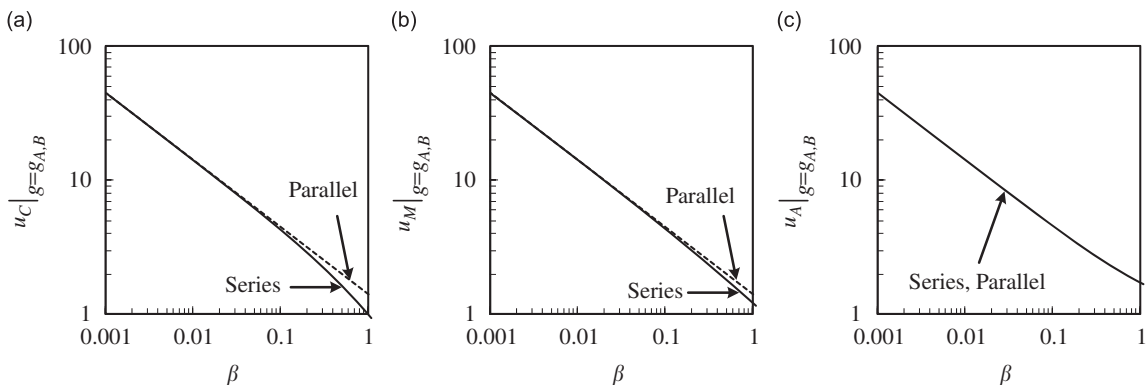

Fig. 9. The relationship between the amplitude at the two fixed points and the equivalent stiffness ratio: (a) in compliance, (b) in mobility, and (c) in accelerance.

used in vibration suppression with piezoelectric elements and LR circuits. From Eqs. (37), (41), and (66), the equivalent mass ratio is given as follows:

$$\mu = \frac{L\Theta^2}{M} = \frac{\beta}{f_{\text{opt}}^2}. \tag{68}$$

The optimum natural frequency ratio f_{opt} approaches 1, and so the values of the mass and stiffness ratios are nearly equal. The performances of mechanical and electrical vibration absorbers can be compared by using the mass and stiffness ratios.

From Eqs. (32)–(34), the stiffness and damping added by the additional electrical system are evaluated by βG_S and βG_P. This paper defines added stiffness ratio γ_K and added damping ratio γ_D as follows:

$$\gamma_K = \begin{cases} \text{Re}(\beta G_S) & \text{(series)}, \\ \text{Re}(\beta G_P) & \text{(parallel)}, \end{cases} \tag{69}$$

$$\gamma_D = \begin{cases} \dfrac{\text{Im}(\beta G_S)}{2g} & \text{(series)}, \\ \dfrac{\text{Im}(\beta G_P)}{2g} & \text{(parallel)}. \end{cases} \tag{70}$$

As an example, γ_K and γ_D with $\beta=0.030$ are shown in Fig. 10. In this example, optimum values of LR circuits in the compliance were adopted. The results of a typical mechanical vibration absorber (MVA) using the same stiffness ratio are also shown in Fig. 10. Around the natural frequency, the added stiffness ratio of a series LR circuit is larger than that of a parallel LR circuit, and the added damping ratios are nearly equal. These are the reasons that the performance of a series LR circuit is small degree better than that of a parallel LR circuit in terms of the compliance and mobility. The added stiffness ratios approach β when g becomes large. The added damping ratio of a series LR circuit approach $\beta \zeta_{S_{\text{opt}}}/f_{\text{opt}}$ when g becomes small. A series LR circuit gives damping to the main system in the frequency range less than the natural frequency.

2.4.2. Comparison of optimum values of inductance

Inductance should be tuned so that the system has an electrical resonance. In this case, the resonance frequency of the electrical system is nearly equal to the natural frequency of the main system. This represents an optimal condition. Because the added stiffness of a series LR circuit is larger than that of a parallel LR circuit, as shown in Fig. 10(a), the optimum natural frequency ratio of a series LR circuit is larger than that of a parallel LR circuit. As a result, the optimum values of the inductance of a series LR circuit are smaller; however, the difference is usually small because of the smallness of the equivalent stiffness ratio β.

2.4.3. Comparison of optimum values of resistance

In general, the equivalent stiffness ratio is much smaller than 1. In this case, the ratio of optimum values of the resistances is given as

$$R_{S_{\text{opt}}} : R_{P_{\text{opt}}} = 2\zeta_{S_{\text{opt}}} \frac{1}{f_{S_{\text{opt}}}} \frac{1}{C_p^S} \frac{1}{\Omega} : \frac{1}{2\zeta_{P_{\text{opt}}}} \frac{1}{f_{P_{\text{opt}}}} \frac{1}{C_p^S} \frac{1}{\Omega} \approx 4\zeta_{S_{\text{opt}}}\zeta_{P_{\text{opt}}} : 1, \tag{71}$$

where $R_{S_{\text{opt}}}$ and $R_{P_{\text{opt}}}$ are the optimum resistances of series and parallel LR circuits, respectively, and $f_{S_{\text{opt}}}$ and $f_{P_{\text{opt}}}$ are the optimum natural frequency ratios of series and parallel LR circuits, respectively. $\zeta_{S_{\text{opt}}}$ and $\zeta_{P_{\text{opt}}}$ are given by Eqs. (57), (61), and (65), and they are usually much smaller than 1; therefore, $R_{P_{\text{opt}}}$ is much larger than $R_{S_{\text{opt}}}$.
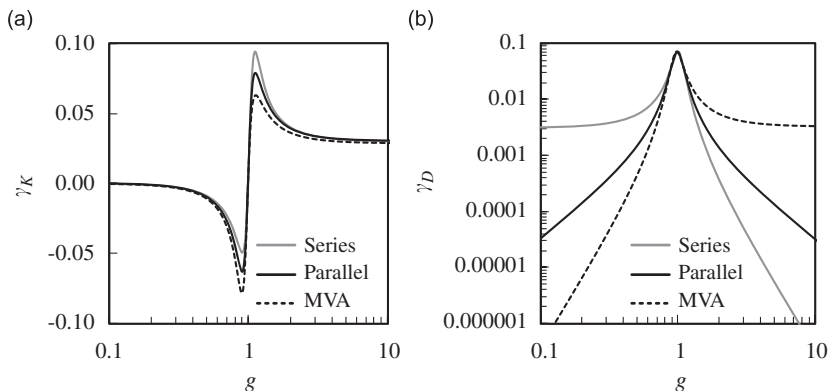

Fig. 10. Frequency characteristics of the added stiffness and damping ratios of series and parallel LR circuits and a typical mechanical vibration absorber using $\beta=0.030$: (a) added stiffness ratio and (b) added damping ratio.

Since the electrical resonance of the additional electrical system suppresses vibration of the host structure, the current which flows back and forth between the inductance and the capacitance should be large. In the method using a series LR circuit, the amplitude of electrical charge becomes large if the resistance is small. By contrast, the amplitude of electrical charge for the method using a parallel LR circuit becomes large if the resistance is large. These are the reasons that $R_{P_{\text{opt}}}$ is much larger than $R_{S_{\text{opt}}}$.

2.4.4. Summary of comparison

A series LR circuit is usually superior to a parallel LR circuit in terms of performance; however, there are some exceptions. When the value of C_p^S is large and $R_{S_{\text{opt}}}$ is small, the performance is greatly decreased because of the variation in the value of the resistance. In other words, the performance of a parallel LR circuit is more robust than that of a series LR circuit because $R_{P_{\text{opt}}}$ is very large. The same thing is adopted for the value of Ω. The circuit should be chosen in consideration of not only performance but also robustness.

2.5. Dielectric loss of a piezoelectric element and internal resistance of an inductor

In practice piezoelectric elements dissipate some energy due to dielectric loss. This phenomenon is caused by the relaxation time of polarization. As shown in Fig. 11(a), the dielectric loss can be expressed by a parallel resistance R_C in the equivalent circuit. R_C is given as follows:

$$R_C = \frac{1}{\omega C_p^T \tan \delta}, \tag{72}$$

where δ is the dielectric loss factor. When $R_C = \infty$, there is no energy loss.

Similarly, inductors also dissipate energy because they have not only inductance but also internal resistance. As shown in Fig. 11(b), the internal resistance can be expressed by a series resistance R_L.

If the dissipated energy due to R_C and R_L is very small, they are negligible. However, sometimes the influence of R_C and R_L cannot be ignored. The models of passive vibration suppression, including R_C and R_L, are shown in Fig. 12. The influence of R_C and R_L is identical to the resistances in the parallel and series LR circuits, respectively. The nondimensional
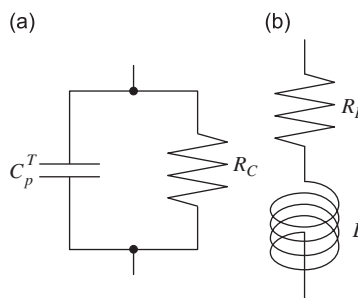

Fig. 11. Equivalent circuit including the dielectric loss of the piezoelectric element and the internal resistance in the inductor: (a) dielectric loss of the piezoelectric element and (b) internal resistance in the inductor.
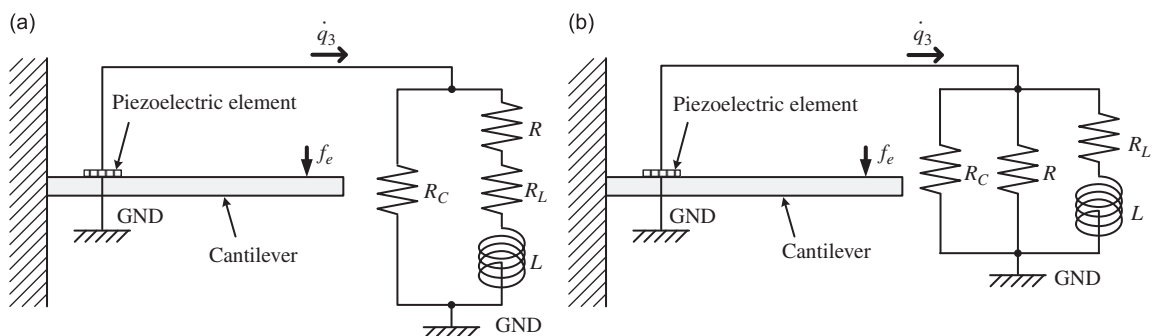

Fig. 12. Schematic diagrams of passive vibration suppression including R_C and R_L: (a) series LR circuit and (b) parallel LR circuit.

compliance then is given as

$$\frac{\varXi}{\varXi_{st}} = \begin{cases} \dfrac{1}{-g^2+1+\beta G_{S2}} & \text{(series)}, \\[3mm] \dfrac{1}{-g^2+1+\beta G_{P2}} & \text{(parallel)}, \end{cases} \tag{73}$$

$$G_{S2} = \frac{-g^2+2j\zeta_1 fg}{(1+4\zeta_1\zeta_C)f^2-g^2+2j(\zeta_1+\zeta_C)fg}, \tag{74}$$

$$G_{P2} = \frac{-g^2+2j\zeta_L fg}{(1+4\zeta_L\zeta_2)f^2-g^2+2j(\zeta_L+\zeta_2)fg}, \tag{75}$$

$$\zeta_C = \frac{1}{2R_C}\sqrt{\frac{L}{C_p^S}}, \quad \zeta_L = \frac{R_L}{2}\sqrt{\frac{C_p^S}{L}}, \quad \zeta_1 = \zeta_S+\zeta_L, \quad \zeta_2 = \zeta_P+\zeta_C. \tag{76–79}$$

In this case, it is impossible to derive the optimum values of the circuit theoretically by use of the two fixed points method because there are no fixed points in Eq. (73). However, the values can be estimated approximately. The practical models are intermediates between the two ideal models shown in Fig. 7. Therefore, the optimum values in the practical models are expected to be close to the optimum values in the ideal models. From Eqs. (53), (58), and (62), the optimum natural frequency ratios in the practical models are expected to approach 1. The total resistance ratios in the practical models are defined as follows:

$$\zeta_T = \begin{cases} \zeta_S+\zeta_L+\zeta_C & \text{(series)}, \\ \zeta_P+\zeta_L+\zeta_C & \text{(parallel)}, \end{cases} \tag{80}$$

From Eqs. (57), (61), and (65), the optimum resistance ratios in the ideal models are almost equal although the values of the resistances are significantly different. It suggests that the optimum resistance ratio does not depend on the position of the resistance. Therefore, the total resistance ratios in the practical models should be tuned to be close to the optimum resistance ratios in the ideal models. The value of the resistance, which should be used in the experiment, can be estimated when the resistance ratios ζ_C and ζ_L are given. If $\zeta_C+\zeta_L$ is larger than the optimum resistance ratio, LR circuits cannot be optimally tuned. Therefore, piezoelectric elements and inductors with small resistance ratios should be chosen.

2.6. Effect of stiffness of adhesive bond

Piezoelectric elements are attached to the target with adhesive bonds. In the preceding subsections, piezoelectric elements were assumed to be fixed to the host structure, and the effect of the adhesive bond was ignored. However, the stiffness of the adhesive bond is generally not large enough to be ignored. The elemental imaginary and perfect equivalent mechanical models including the stiffness of adhesive bonds are shown in Fig. 13. Here k_{a1} is the stiffness of the adhesive bond, and x_{a1} is the displacement of the connecting point between the adhesive bond and the piezoelectric element. From these equivalent mechanical models, the equilibria of force are given as follows:

$$F_1 = k_{a1}(x_1-x_{a1}), \tag{81}$$

$$k_{a1}(x_1-x_{a1}) = k_p x_{a1} + k_z\left(x_{a1}-\frac{q_3}{\theta_p}\right), \tag{82}$$

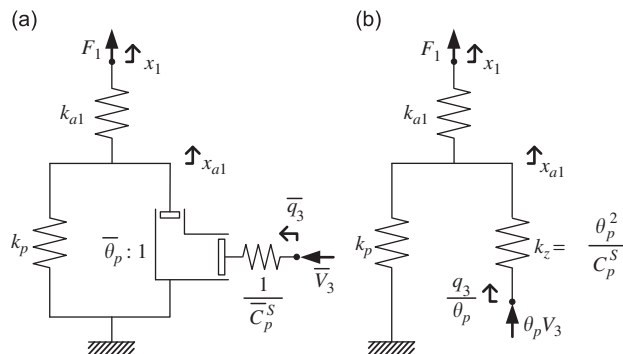$$k_z\left(x_{a1}-\frac{q_3}{\theta_p}\right) = -\theta_p V_3. \tag{83}$$

Fig. 13. Elemental equivalent mechanical models with the stiffness of the adhesive bond: (a) imaginary model and (b) perfect model.

Eqs. (81)–(83) are equivalently transformed into the following equations:

$$F_1 = k'_p x_1 + k'_z \left(x_1 - \frac{q_3}{\theta'_p} \right), \tag{84}$$

$$k'_z \left(x_1 - \frac{q_3}{\theta'_p} \right) = -\theta'_p V_3, \tag{85}$$

where

$$k'_p = \frac{k_{a1}}{k_{a1} + k_p} k_p, \tag{86}$$

$$k'_z = \frac{k_{a1}^2}{(k_{a1} + k_p + k_z)(k_{a1} + k_p)} k_z, \tag{87}$$

$$\theta'_p = \frac{k_{a1}}{k_{a1} + k_p} \theta_p. \tag{88}$$

The equivalent mechanical models are transformed into Fig. 14. Here C'_p is given as

$$C'_p = \frac{k_{a1} + k_p + k_z}{k_{a1} + k_p} C_p^S. \tag{89}$$

From Eq. (86), the apparent elastic compliance is defined as follows on the assumption that length, width, and thickness of the piezoelectric element are constant

$$s'^E_{11} = \frac{k_{a1} + k_p}{k_{a1}} s^E_{11}. \tag{90}$$

Apparently the value of the elastic compliance is varied by the stiffness of the adhesive bond; however, the values of the piezoelectric constant d_{31} and the electrical permittivity ε^T_{33} are not varied at all. It is difficult to predict the value of k_{a1} accurately because the value depends on not only the longitudinal shear strength of the adhesive bond but also the amount and the distribution of the adhesive bond. From Eq. (90), the apparent Young's modulus of the piezoelectric element is decreased, and the decrease causes performance deterioration. Therefore, the longitudinal shear strength of the adhesive bond should be high.

2.7. Effect of restraint in width direction

In the preceding subsections, the properties of the piezoelectric element in the width direction are ignored for simplicity. If Poisson's ratio of the piezoelectric element is very small and the piezoelectric element is not bound in width direction, there is no issue. However, Poisson's ratio is generally not so small, and piezoelectric elements are usually restrained not only in the longitudinal direction but also in the width direction by the adhesive bond. To formulate the properties of the attached piezoelectric element accurately, the restraint in width direction must be taken into consideration. As shown in Fig. 15(a), the restraint of the piezoelectric element in width direction can be expressed by the stiffness of the adhesive bond k_{a2} as well as in longitudinal direction. Since the effect of the restraint in longitudinal direction has already been studied in the preceding subsection, only the effect of the restraint in width direction should be investigated in this subsection. The restraint model (in width direction only) is shown in Fig. 15(b). The piezoelectric constitutive equations are given as

$$S_1 = s^E_{11} T_1 - v_p s^E_{11} T_2 + d_{31} E_3, \tag{91}$$

$$0 = \frac{T_2 l_p t_p}{k_{a2}} + w_p (-v_p s^E_{11} T_1 + s^E_{11} T_2 + d_{31} E_3), \tag{92}$$

$$D_3 = d_{31} T_1 + d_{31} T_2 + \varepsilon^T_{33} E_3, \tag{93}$$
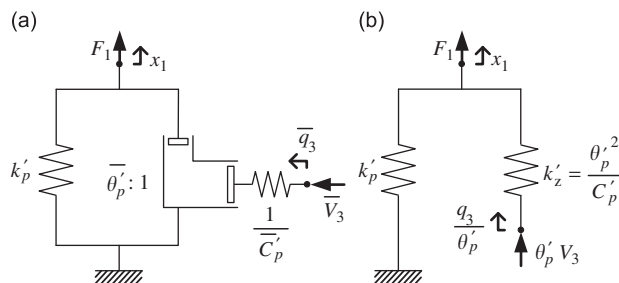

Fig. 14. Simplified elemental equivalent mechanical models with the stiffness of the adhesive bond: (a) imaginary model and (b) perfect model.
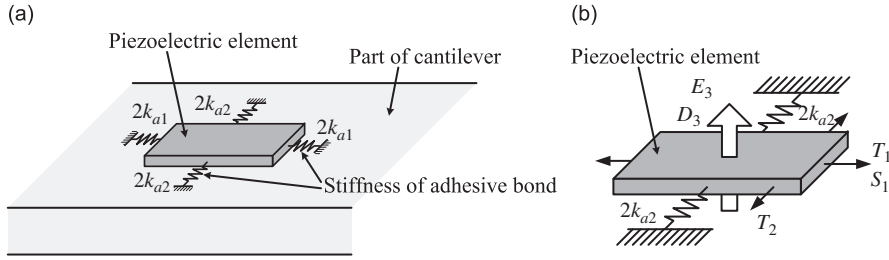
Fig. 15. Theoretical models of a piezoelectric element restrained by stiffness of the adhesive bond: (a) full restraint model and (b) restraint model only in width direction.

where ν_p is Poisson's ratio. The piezoelectric element was assumed to be isotropic in longitudinal and width directions. The subscript 2 denotes the width direction. Eqs. (91)–(93) are transformed as follows:

$$S_1 = s_{11}''^E T_1 + d_{31}'' E_3, \tag{94}$$

$$D_3 = d_{31}'' T_1 + \varepsilon_{33}''^T E_3, \tag{95}$$

where

$$s_{11}''^E = s_{11}^E - \frac{(\nu_p s_{11}^E)^2}{s_{11}^E + s_{a2}}, \tag{96}$$

$$d_{31}'' = d_{31}\left(1 + \frac{\nu_p s_{11}^E}{s_{11}^E + s_{a2}}\right), \tag{97}$$

$$\varepsilon_{33}''^T = \varepsilon_{33}^T - \frac{d_{31}^2}{s_{11}^E + s_{a2}}, \tag{98}$$

$$s_{a2} = \frac{1}{k_{a2}}\frac{l_p t_p}{w_p}. \tag{99}$$

From Eqs. (96)–(98), the elastic compliance, the piezoelectric constant, and the electrical permittivity in Eqs. (1) and (2) are turned into $s_{11}''^E$, d_{31}'', and $\varepsilon_{33}''^T$, apparently because of the restraint in width direction. Usually the changes are larger, and all of these changes improve the performance of the piezoelectric elements. It is also difficult to obtain the accurate value of k_{a2} theoretically; however, it can theoretically be said that piezoelectric elements should also be fixed in the width direction.

3. Validation of theoretical analysis by simulation and experiment

3.1. Validation of optimum value of resistance

To validate the effectiveness of the new formulations of the resistance, simulations were carried out. The simulated magnitudes of the nondimensional compliance using series and parallel LR circuits with $\beta = 0.01000$ are shown in Fig. 16. Here ζ_{opt} denotes the optimum resistance ratio derived in this paper, and ζ_{old} denotes the resistance ratio adopted as an approximate optimum resistance ratio in previous papers [3–6]. The values of the resistance ratios are shown in Table 1. It is shown that the optimum resistance ratios formulated in this paper are superior to previous ones.

In this paper, the optimum resistance ratios were defined by root mean square of ζ_A and ζ_B. The values of the resistance ratios derived by arithmetic average, geometric average, and root mean square are written in Table 2. It is shown that the results of three kinds of averages are almost equal, and these differences do not have influence on the frequency response functions.

3.2. Validation of optimum values in mobility and accelerance

3.2.1. Experimental apparatus

A schematic diagram of the experimental apparatus used in this study is shown in Fig. 17. The material properties of the apparatus are written in Tables 3 and 4. Here m_{acc} is the mass of the accelerometer and x_{acc} is the location of the accelerometer. Two pieces of piezoelectric elements were attached to the cantilever; one was used for vibration suppression and the other for excitation of the beam. Both conductive and non-conductive adhesive bonds were used. The conductive type was used to simplify wiring, and the non-conductive type for fixing and electrical insulation. Specifically,
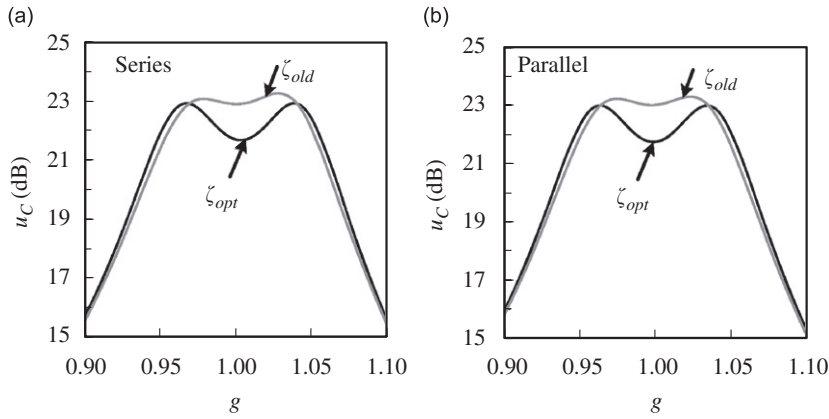
Fig. 16. Simulated magnitudes of the nondimensional compliance with two kinds of the values of the resistance and $\beta=0.01000$: (a) series LR circuit and (b) parallel LR circuit.

Table 1
The resistance ratios used in the simulations shown in Fig. 16.

	ζ_{old}	ζ_{opt}
Series LR circuit	0.07036	0.06108
Parallel LR circuit	0.07089	0.06139

Table 2
The resistance ratios derived by arithmetic average, geometric average, and root mean square.

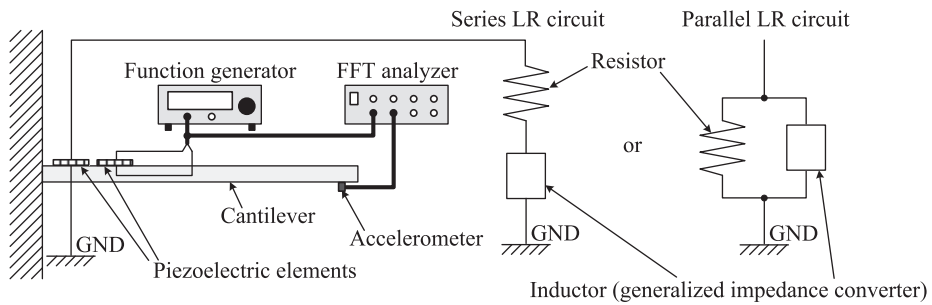|	Point A	Point B	Arithmetic average	Geometric average	Root mean square
Series LR circuit	0.06320	0.05890	0.06105	0.06101	0.06108
Parallel LR circuit	0.06211	0.06066	0.06139	0.06138	0.06139

Fig. 17. Schematic diagram of the experimental apparatus.

a drop of the conductive adhesive bond was placed on the center of the piezoelectric elements and it was surrounded by the non-conductive adhesive bond. An inductor made by a generalized impedance converter was used in this experiment because the size of an actual coil is too large. In this experiment, the fundamental vibration mode of the cantilever was suppressed. The equivalent stiffness ratio, the capacitance of the piezoelectric element, the modal stiffness, and the modal damping coefficient, which were experimentally measured, are shown in Table 5 [14]. Here, the superscript x denotes that the values were obtained experimentally. The modal stiffness were derived as

$$K^x = (2\pi F_S^x)^2, \tag{100}$$

where F_S^x is the natural frequency of the fundamental vibration mode when the electrodes of the piezoelectric element are shorted in the experiment. The electromechanical coupling coefficient derived by Eq. (37) and the modal mass are also written in Table 5. The experimental result of the magnitude of the nondimensional compliance with short circuit is shown in Fig. 18.

Table 3
Material properties of the cantilever and the accelerometer.

Cantilever		
Length	l_b	0.280 m
Width	w_b	0.0500 m
Thickness	t_b	0.00300 m
Density	ρ_b	7900 kg/m^3
Young's modulus	E_b	2.06×10^{11} N/m^2
Accelerometer		
Mass	m_{acc}	0.20 g
Location	x_{acc}	0.270 m

Table 4
Material properties of the piezoelectric elements.

Length	l_p	0.0320 m
Width	w_p	0.0220 m
Thickness	t_p	0.000230 m
Density	ρ_p	8050 kg/m^3
Elastic compliance	s_{11}^E	1.55×10^{-11} m^2/N
Young's modulus	E_p	6.45×10^{10} N/m^2
Piezoelectric constant	d_{31}	2.30×10^{-10} C/N
Electrical permittivity	ε_{33}^T	2.35×10^{-8} F/m
Poisson's ratio	ν_p	0.30
Dielectric loss factor	δ	0.020
Location of the piezoelectric element for vibration suppression	(x_ℓ, x_r)	(0.0050, 0.0370) m
Location of the piezoelectric element for excitation	(x_ℓ, x_r)	(0.0400, 0.0720) m

Table 5
Experimentally measured parameters of the cantilever with the two piezoelectric elements.

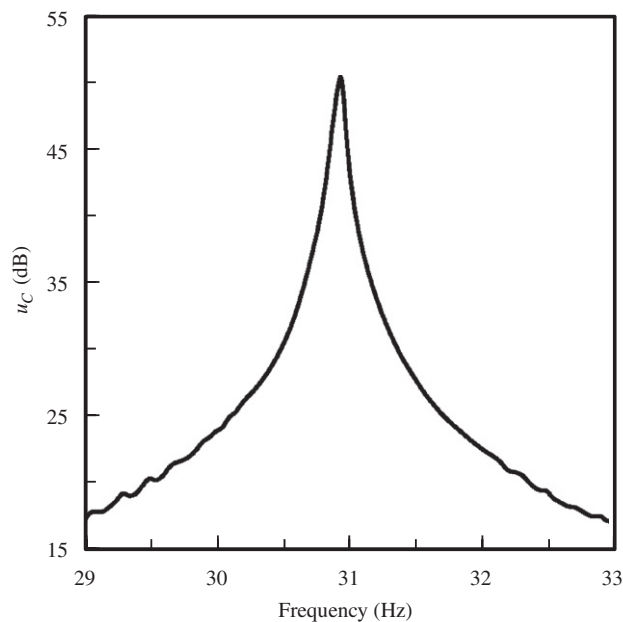|		
Equivalent stiffness ratio	β^x	0.00411
Capacitance	C_p^x	0.0480 μF
Electromechanical coupling coefficient	Θ_x	0.00273 N/V
Modal stiffness	K^x	37,800 N/m
Modal damping coefficient	D^x	0.567 N s/m
Modal mass	M	1.00 kg

Fig. 18. The experimental result of the magnitude of the nondimensional compliance with short circuit.
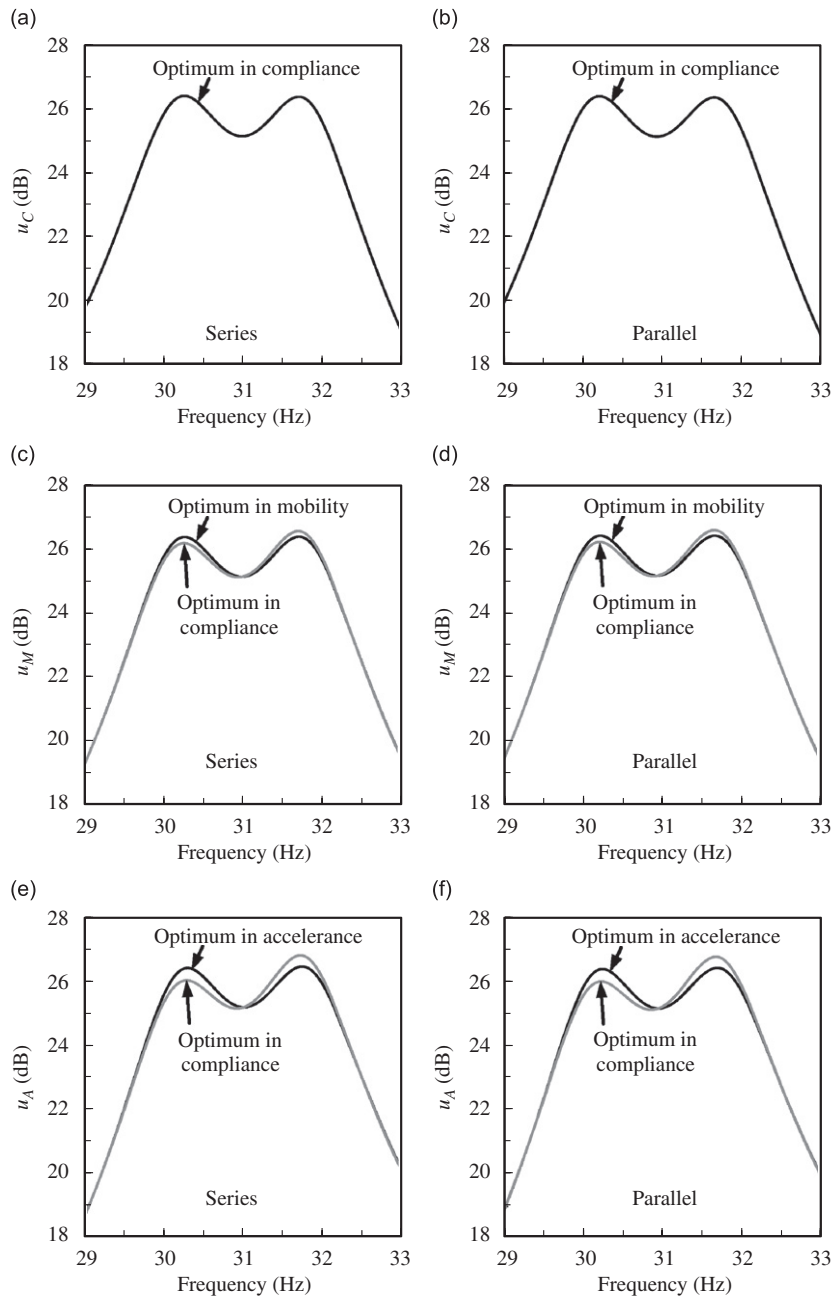
Fig. 19. Simulated results of magnitudes of the nondimensional compliance, mobility, and accelerance using the optimum values: (a) compliance with series LR circuit, (b) compliance with parallel LR circuit, (c) mobility with series LR circuit, (d) mobility with parallel LR circuit, (e) accelerance with series LR circuit, and (f) accelerance with parallel LR circuit.

3.2.2. Simulated and experimental results

The simulated and experimental magnitudes of the nondimensional compliance, mobility, and accelerance using optimum values in compliance, mobility, and accelerance, respectively, are shown in Figs. 19 and 20, respectively. The values of the material properties used in the simulations are the experimental ones written in Table 5. The damping coefficient of the cantilever was ignored in the theoretical analysis; however, it was included in these simulations. In the mobility and the accelerance, the results using the LR circuit which was tuned optimally in terms of the compliance are also shown. The theoretical optimum values and the experimental values of the LR circuit are listed in Tables 6 and 7, respectively. These frequency response functions change sensitively depending on the value of the inductance. The magnitude relation of the inductance values in the experiment agrees well with the simulated ones. The reason why the
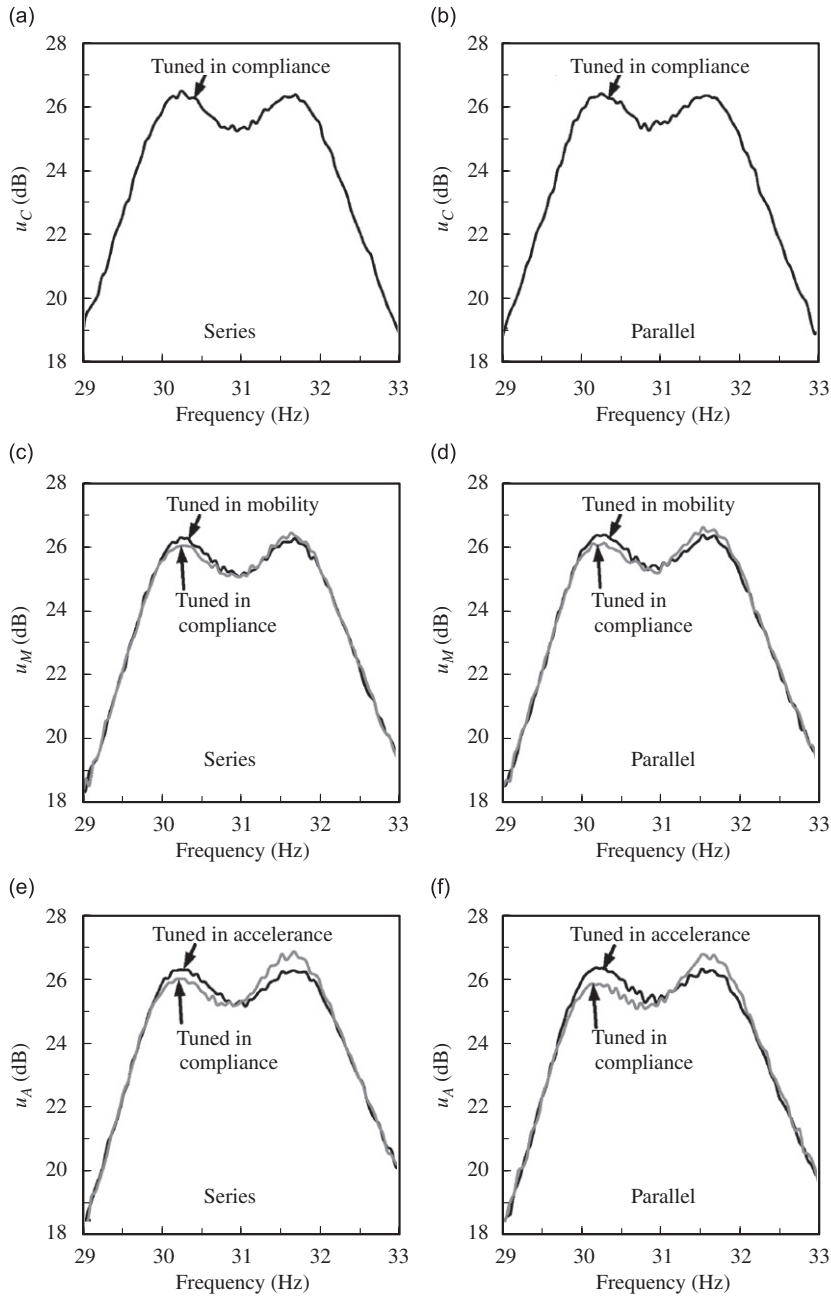
Fig. 20. Experimental results of magnitudes of the nondimensional compliance, mobility, and accelerance using the optimum values: (a) compliance with series LR circuit, (b) compliance with parallel LR circuit, (c) mobility with series LR circuit, (d) mobility with parallel LR circuit, (e) accelerance with series LR circuit, and (f) accelerance with parallel LR circuit.

Table 6
Theoretical optimum values of the LR circuit in compliance, mobility, and accelerance.

	Compliance	Mobility	Accelerance
Series LR circuit			
L_{opt}	549 H	548 H	547 H
R_{opt}	$8.39 \times 10^3 \, \Omega$	$8.37 \times 10^3 \, \Omega$	$8.36 \times 10^3 \, \Omega$
Parallel LR circuit			
L_{opt}	552 H	551 H	550 H
R_{opt}	$1.36 \times 10^6 \, \Omega$	$1.36 \times 10^6 \, \Omega$	$1.36 \times 10^6 \, \Omega$

Table 7
Experimental values of the LR circuit in compliance, mobility, and accelerance.

	Compliance	Mobility	Accelerance
Series LR circuit			
L	553 H	552 H	550 H
R	$5.10 \times 10^3 \, \Omega$	$5.10 \times 10^3 \, \Omega$	$5.10 \times 10^3 \, \Omega$
Parallel LR circuit			
L	558 H	555 H	555 H
R	$2.41 \times 10^6 \, \Omega$	$2.41 \times 10^6 \, \Omega$	$2.41 \times 10^6 \, \Omega$

Table 8
Values of R_C, R_L, and various resistance ratios in the experiment and theoretical optimum resistance ratios.

	Series LR		Parallel LR
Experimental values			
R_C		$3.61 \times 10^6 \, (3.6 \times 10^6) \, \Omega$	
R_L		37 Ω	
ζ_C	0.0149		0.0149
ζ_L	0.00017		0.00017
ζ_S	0.0238		–
ζ_P	–		0.0224
ζ_T	0.0389		0.0375
Theoretical optimum values			
ζ_{opt}	0.0392		0.0393

values of the inductance are large is that the capacitance value of the piezoelectric element is small. The theoretical optimum values and the experimental ones of the resistance are much different. The detail is described in the following subsection. It can be said that optimum values in the proper frequency response function should be adopted.

3.3. Various resistance ratios in experiment

The difference between the theoretical and experimental resistance values in Tables 6 and 7 is due to the dielectric loss of the piezoelectric element and the internal resistance of the inductor made using the generalized impedance converter. R_C and R_L measured experimentally are written in Table 8. Here R_C was measured at $\omega = (K^x)^{1/2}$. R_C obtained by Eq. (72) and $\omega = (K^x)^{1/2}$ is also written in Table 8 in parentheses. The various resistance ratios in the experiment and the theoretical optimum resistance ratios are given in Table 8. Only the values with respect to compliance are listed because the difference among compliance, mobility, and accelerance is small. The experimental total resistance ratios and the theoretical optimum resistance ratios agree well. These results imply that the optimum resistance value in the experiment can be estimated and dielectric loss of piezoelectric elements should be taken into consideration when the material of the piezoelectric elements is determined.

3.4. Investigation of stiffness of adhesive bond in experiment

To investigate the effect of the adhesive bond, a calculation model was constructed as shown in Fig. 21. The accurate curvature of the mode shape of the cantilever can be derived by the calculation model. The cantilever was divided into 280 segments, and the equivalent mass and stiffness of each segment were theoretically obtained. The stiffness and the mass of the two piezoelectric elements and the mass of the accelerometer were taken into consideration. The theoretically calculated equivalent stiffness ratio β^c, capacitance C_p^c, modal stiffness K^c, and modal electromechanical coupling coefficient Θ^c using various k_{a1} and k_{a2} are shown in Fig. 22. The material parameters listed in Tables 3 and 4 were used in this calculation. Note that the axes of C_p^c are reversed. The results show that the equivalent stiffness ratio and the capacitance of the piezoelectric element are greatly affected by the stiffness of the adhesive bond. Those values are varied significantly around $k_{a1} = k_p = 1.02 \times 10^7 \, \text{N/m}$ and $k_{a2} = k_{p2} = 2.16 \times 10^7 \, \text{N/m}$. Here

$$k_{p2} = E_p \frac{l_p t_p}{w_p}. \tag{101}$$

The theoretically calculated combinations of k_{a1} and k_{a2}, which satisfy either $\beta^c = 0.00411$ or $C_p^c = 0.0480\,\mu F$, are shown in Fig. 23. The values of the intersection point are $k_{a1} = 1.26 \times 10^8\,\text{N/m}$ and $k_{a2} = 7.76 \times 10^7\,\text{N/m}$. These are the estimated values of k_{a1} and k_{a2} in the experimental apparatus. Both k_{a1} and k_{a2} are larger than k_p and k_{p2}, respectively; however, the value of the equivalent stiffness ratio can still be improved by using stiffer adhesive bonds.

The reason why k_{a2} is smaller than k_{a1} is that the distribution of the adhesive bond were not uniform in the experimental apparatus. An extreme example is shown in Fig. 24. In this example, the piezoelectric element is restrained only in the longitudinal direction. By comparison, k_{a1} and k_{a2} become the same value if the adhesive bond is uniformly spread on the entire piezoelectric element. Since the difference between the estimated values of k_{a1} and k_{a2} is not so large, it is reasonable to suppose that the theoretical analysis with respect to adhesive bonds is effective.
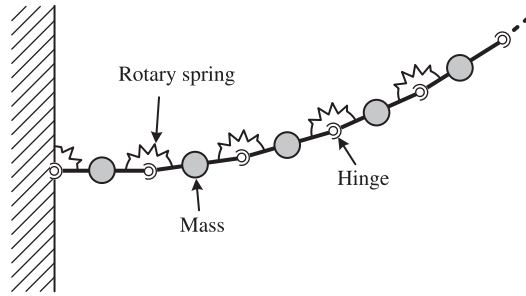

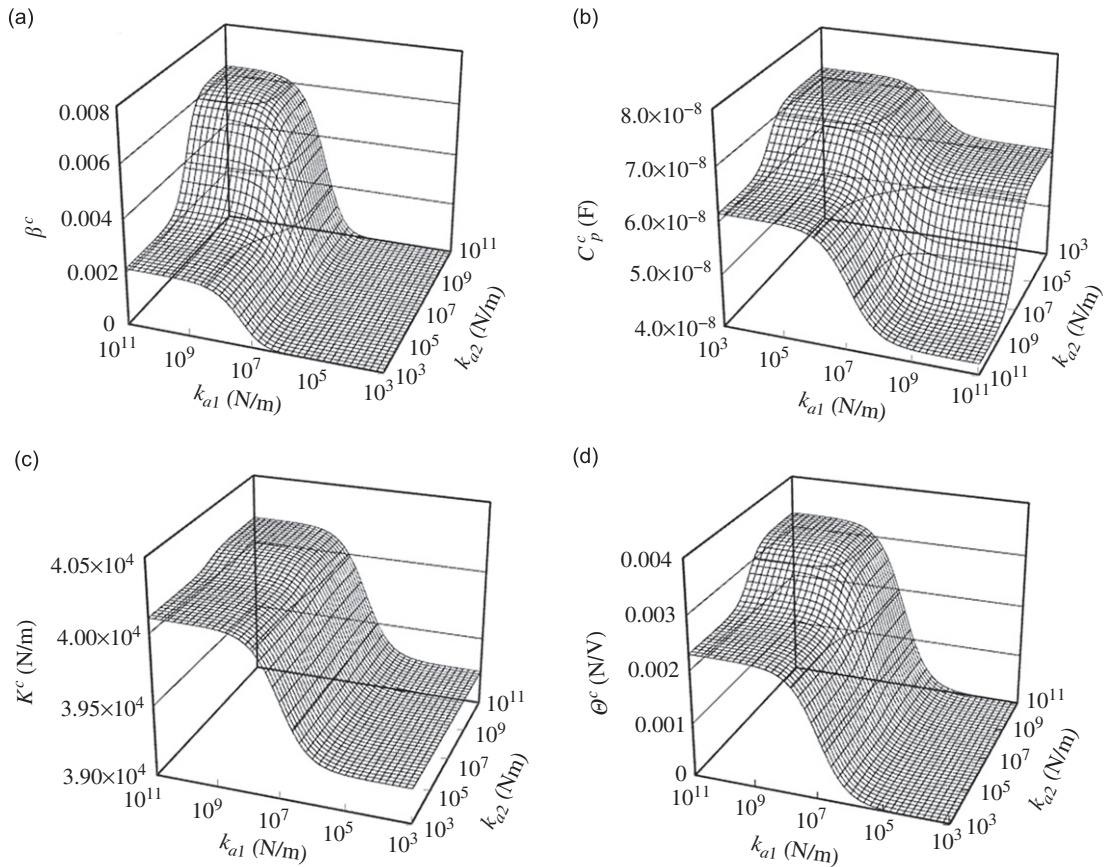**Fig. 21.** Calculation model of the cantilever with the piezoelectric elements to derive the mode shape.

Fig. 22. Theoretically calculated parameters of the cantilever with the piezoelectric elements using various k_{a1} and k_{a2}: (a) equivalent stiffness ratio, (b) capacitance, (c) modal stiffness, and (d) electromechanical coupling coefficient.
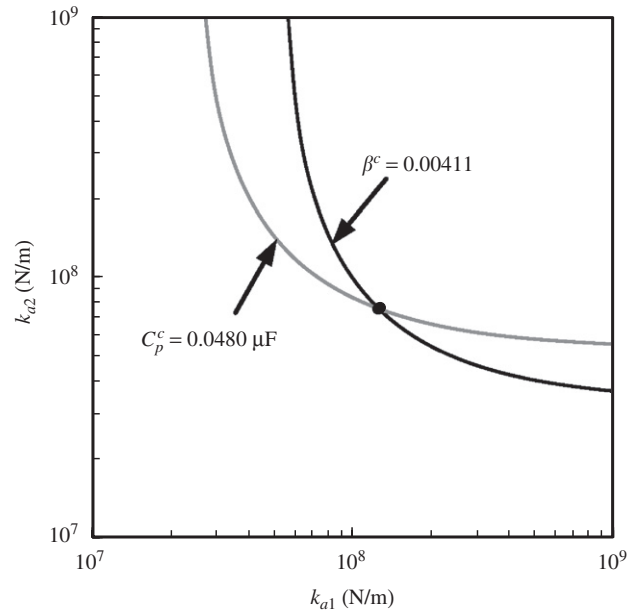
Fig. 23. Theoretically calculated results of the combinations of k_{a1} and k_{a2} which satisfy β^c=0.00411 and $C_p^c = 0.0480\,\mu F$, respectively.
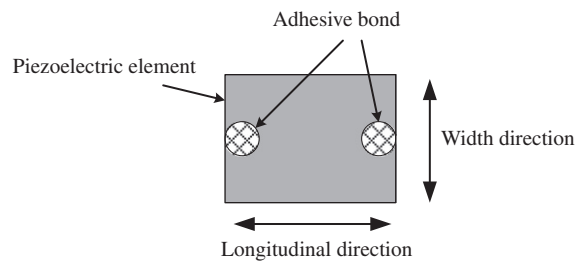

Fig. 24. An extreme example of the distribution of the adhesive bond.

4. Conclusion

The governing equations for passive vibration suppression with series and parallel LR circuits were derived using the new equivalent mechanical model of a piezoelectric element. The optimum values of the series and the parallel LR circuits were formulated by using the two fixed points method not only in terms of compliance but also in terms of mobility and accelerance. The difference between the series and parallel LR circuits was investigated theoretically. The effects of the dielectric loss of the piezoelectric elements, the internal resistance of the inductor, and the stiffness of adhesive bonds were theoretically investigated. The theoretical analysis was validated through numerical simulations and experiments. The performance of the passive vibration suppression technique using LR circuits was determined based on the value of the equivalent stiffness ratio as well as the mass ratio in typical mechanical vibration absorbers. The series LR circuit is superior to the parallel one in terms of compliance and mobility. However, the parallel LR circuit is superior to the series one in terms of robustness with respect to the variation of the resistance. Therefore, it is necessary to use two kinds of LR circuits properly according to the host structure and the piezoelectric element. This work demonstrated that the total resistance ratio, which includes the dielectric loss of the piezoelectric element and the internal resistance of the inductor, should be tuned to be equal to the optimum resistance ratio, and an adhesive bond with high longitudinal shear strength should be used.

Acknowledgement

References

[1] R.L. Forward, Electronic damping of vibrations in optical structures, *Applied Optics* 18 (5) (1979) 690–697.
[2] J.J. Dosch, D.J. Inman, E. Garcia, A self-sensing piezoelectric actuator for collocated control, *Journal of Intelligent Material Systems and Structures* 3 (1992) 166–185.
[3] N.W. Hagood, A. Von Flotow, Damping of structural vibrations with piezoelectric materials and passive electrical networks, *Journal of Sound and Vibration* 146 (2) (1991) 243–268.
[4] C.H. Park, Dynamics modeling of beams with shunted piezoelectric elements, *Journal of Sound and Vibration* 268 (1) (2003) 115–129.
[5] S.Y. Wu, Piezoelectric shunts with a parallel R-L circuit for structural damping and vibration control, *Proceedings of the SPIE 2720*, San Diego, February 1996, pp. 259–269.
[6] C.H. Park, D.J. Inman, A uniform model for series R-L and parallel R-L shunt circuits and power consumption, *Proceedings of the SPIE 3668*, California, March 1999, pp. 797–804.
[7] K. Yamada, H. Matsuhisa, H. Utsuno, Passive vibration suppression using two inductances and piezoelectric elements, *Proceedings of the 12th Asia Pacific Vibration Conference*, Sapporo, August 2007, CD-ROM 114.
[8] G.S. Agnes, Development of a modal model for simultaneous active and passive piezoelectric vibration suppression, *Journal of Intelligent Material Systems and Structures* 6 (1995) 482–487.
[9] M.S. Tsai, K.W. Wang, On the structural damping characteristics of active piezoelectric actuators with passive shunt, *Journal of Sound and Vibration* 221 (1) (1999) 1–22.
[10] K. Adachi, Y. Awakura, T. Iwatsubo, Hybrid piezoelectric damping for structural vibration suppression, *Journal of Intelligent Material Systems and Structures* 15 (2004) 795–801.
[11] K. Yamada, H. Matsuhisa, H. Utsuno, J.G. Park, Hybrid vibration suppression of flexible structures using piezoelectric elements and analog circuits, *JSME Journal of Environment and Engineering* 3 (2) (2008) 424–435.
[12] J. Ormondroyd, J.P. Den Hartog, The theory of the dynamic vibration absorber, *Transactions of the American Society of Mechanical Engineers* 50 (7) (1928) 9–22.
[13] H.H. Law, P.L. Rossiter, G.P. Simon, L.L. Koss, Characterization of mechanical vibration damping by piezoelectric materials, *Journal of Sound and Vibration* 197 (4) (1996) 489–513.
[14] K. Yamada, H. Matsuhisa, H. Utsuno, J.G. Park, Precise measurement technique of the electromechanical coupling coefficient of piezoelectric elements, *Proceedings of the 8th International Conference on Motion and Vibration Control*, Daejeon, August 2006, Flash memory MA1-3.